Available online at www.sciencedirect.com

ScienceDirect

journal homepage: www.elsevier.com/locate/he

$TiFe_{0.85}Mn_{0.05}$ alloy produced at industrial level for a hydrogen storage plant

Jussara Barale [a], *Erika M. Dematteis* [a,b], *Giovanni Capurso* [c,1], *Bettina Neuman* [d], *Stefano Deledda* [e], *Paola Rizzi* [a], *Fermin Cuevas* [b], *Marcello Baricco* [a,*]

[a] *Department of Chemistry and NIS - INSTM, University of Turin, Via Pietro Giuria 7, 10125 Torino, Italy*
[b] *Univ. Paris Est Creteil, CNRS, ICMPE, UMR7182, 2-8 rue Henri Dunant, 94320 Thiais, France*
[c] *Institute of Hydrogen Technology, Helmholtz-Zentrum Hereon, Max-Plank-Straße 1, 21502 Geesthacht, Germany*
[d] *GKN Sinter Metals Engineering GmbH, Krebsöge 10, D-42477 Radevormwald, Germany*
[e] *Institute for Energy Technology, Instituttveien 18, 2007 Kjeller, Norway*

HIGHLIGHTS

- $TiFe_{0.85}Mn_{0.05}$ alloy was prepared at industrial level and deeply characterized.
- Industrial preparation strongly affects the hydrogen sorption properties.
- $TiFe_{0.85}Mn_{0.05}$ shows suitable properties for a large-scale storage system.
- $TiFe_{0.85}Mn_{0.05}$ is activated in mild conditions, stable over cycling and poisoning.

GRAPHICAL ABSTRACT

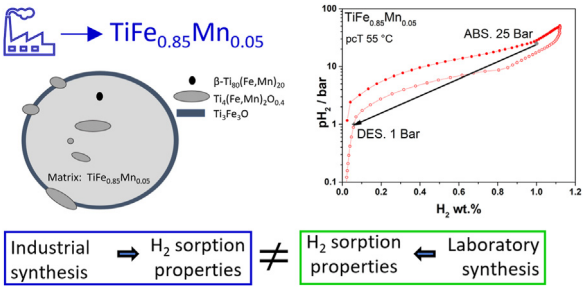

ARTICLE INFO

Article history:
Received 13 April 2022
Received in revised form
6 June 2022
Accepted 28 June 2022
Available online 12 August 2022

Keywords:
Hydrogen storage
Metal hydride
Intermetallic compound

ABSTRACT

Moving from basic research to the implementation of hydrogen storage system based on metal hydride, the industrial production of the active material is fundamental. The alloy $TiFe_{0.85}Mn_{0.05}$ was selected as H_2-carrier for a storage plant of about 50 kg of H_2. In this work, a batch of 5 kg of $TiFe_{0.85}Mn_{0.05}$ alloy was synthesized at industrial level and characterized to determine the structure and phase abundance. The H_2 sorption properties were investigated, performing studies on long-term cycling study and resistance to poisoning. The alloy absorbs and desorbs hydrogen between 25 bar and 1 bar at 55 °C, storing 1.0H_2 wt.%, displaying fast kinetic, good resistance to gas impurities, and storage stability over 250 cycles. The industrial production promotes the formation of a passive layer and a high amount of secondary phases, observing differences in the H_2 sorption behaviour compared to samples prepared at laboratory scale. This work highlights how

* *Corresponding author.*
E-mail address: marcello.baricco@unito.it (M. Baricco).
[1] Present address: Department of Polytechnic Engineering and Architecture, University of Udine, Via Cotonificio 108, 33100 – Udine, Italy.

https://doi.org/10.1016/j.ijhydene.2022.06.295

TiFe-alloys
Industrial production

hydrogen sorption properties of metal hydrides are strictly related to the synthesis method.

Introduction

Hydrogen is a promising widespread energy vector, and its efficient storage is a crucial step for its usage in large scale. Metal hydrides (MHs) allow storing H_2 at mild conditions, *e.g.* $\leq$ 30 bar and room temperature, resulting in a more efficient and safer solution compared to compressed and liquefied H_2. A huge number of alloys has been investigated as hydrides forming materials [1–3], but only few storage devices are commercially available, nowadays. Bellosta von Colbe et al. reported MH-storage systems for stationary and mobile applications, presenting future perspectives and highlighting their potential in stationary uses for smart-grid and off-grid energy management [4]. Intermetallic compounds (IMCs) are good candidates for these types of applications, since they can absorb and desorb H_2 at mild pressures and temperatures, being integrated with Proton Exchange Membrane (PEM) Electrolysers (EL) and PEM Fuel Cells (FC). These compounds generally have low gravimetric hydrogen capacity (<2H_2 wt.%), implying a large mass of carrier needed to store kilograms of H_2, coupled with high volumetric density (>80 kgH_2/m^3). Because in stationary uses there are few limitations on the system weight, but a strong request for low volumes, IMCs are suitable materials to be employed in fixed hydrogen storage systems, *e.g.* for the management of intermittent renewable energies.

The TiFe IMC has a big potential for widespread use in stationary applications, since it stores hydrogen at mild pressures and temperatures (*e.g.* 10–20 bar and 30–70 °C), being easily integrated with electrolyser and fuel cell [5,6]. Moreover, it is inexpensive, non-toxic and the raw materials are abundant [7–9]. TiFe has a cubic CsCl-type structure, space group $Pm\bar{3}m$ with a cell parameter depending on Ti at.%, i.*e.* from 2.974 to 2.978 Å for a Ti-content from 49.5% to 52.5%, respectively [8,10,11]. After dissolving hydrogen in solid solution (α-TiFe$H_{0.06}$), it forms two subsequent hydrides, visible in the pressure-composition-Temperature (pcT) curves through two consequent plateaux: a monohydride (β-TiFeH) and a dihydride (γ-TiFeH_2), presenting a maximum gravimetric capacity close to 2H_2 wt.% [9,12]. A drawback is its hard activation, which usually requires high temperatures (*e.g.* 400 °C) [7,12,13] and/or high hydrogen pressures (up to 100 bar) [14]. A strategy to overcome this problem and to tailor H_2 sorption properties involves the substitution of Ti and/or Fe with other elements [15–26], and/or the enrichment of Ti in the composition [24,27–29], to promote the formation of secondary phases that have been found to help in the activation process. A large hysteresis gap between absorption and desorption pressure is usually observed, which depends on the sample history (*e.g.* synthesis and activation) [12]. A comprehensive overview of the properties of TiFe and TiFe-based alloys was reported in two recent reviews by Sujan [8] et al. and Dematteis et al. [24]. Mn is a common substitution for Fe in TiFe, forming $TiFe_xMn_{(1-x)}$ alloys [17,30]. As reported by Johnson et al. [30], Mn containing compounds showed a decrease in the equilibrium pressures for hydrogen sorption and an increase in cell dimension, with respect to the original TiFe compound. On the contrary, no significant changes in gravimetric capacity were evidenced up to x = 0.70. Mn additions result in the occurrence of sloping plateaux in the pcT-curves. These can be limited by suitable annealings, which promote also a reduction of the hysteresis gap [30]. Challet et al. [31], prepared and studied $Ti(Fe_{0.70+x}Mn_{0.20-x})$ alloys, with x = 0.00, 0.05, 0.10 and 0.15. Samples were synthesized by induction melting, annealed at 1000 °C for 1 week and then quenched. For the first hydrogenation, activation was not necessary for any sample and pcT-curves presented two distinct plateaux, with a limited slope. Increasing the Fe-content, the unit cell dimension progressively decreased, coupled with an increase of the plateaux pressure from 4 to 20 bar at 65 °C. All alloys displayed fast kinetics and no relevant changes on gravimetric capacity were reported, compared to the parent TiFe. In a recent study, Dematteis et al. [32] investigated the storage properties of a series of TiFe-based compounds and evaluated the effect of Mn and Ti substituting Fe in the alloy, by mapping Ti:Fe ratio from 1.0:1.0 to 1.0:0.9 and by varying the Mn content between 0 and 5 at.%. Samples were prepared at laboratory scale, similarly to Challet et al. [31]. Secondary phases of Ti_4Fe_2O-type, β-Ti-type or $TiFe_2$ were detected, always with abundance below 10 wt.%. The occurrence of the latter two compounds agrees with the TiFe phase diagram [33]. In fact, Ti-rich compositions, as compared to stoichiometric TiFe, form β-Ti-rich solid solution precipitates whereas, for Ti-poor compositions, the formation of $TiFe_2$ precipitates is expected. It is worth noting that the oxide was detected only in Ti-rich compositions, i.*e.* with Ti > 50 at.%, due to the high reactivity of Ti with oxygen, the latter being incorporated during sample preparation and/or already present in the starting materials [34,35]. Nevertheless, it was observed that a suitable quantity of secondary phases helped the activation process, but an excess causes a decrease in the gravimetric capacity. The addition of Mn in TiFe-based alloys increases the unit cell dimension, and a linear dependence was observed between the cell dimension and the equilibrium pressure for hydrogen sorption, as well as the pressure step between two plateaux in the pcT-curves and the hysteresis gap [30,31]. Authors concluded that the $TiFe_{0.85}Mn_{0.05}$ composition is the most promising for practical applications, thanks to an easy activation with 7 h of incubation time under H_2 at 25 bar and 25 °C, which results in fast absorption kinetics and a reversible capacity of 1.63H_2 wt.%.

Thanks to the suitable H_2 sorption properties reported for $TiFe_{0.85}Mn_{0.05}$ [31,32], this composition was selected as H_2-carrier for a plant designed to store up to 50 kg of H_2 [36]. The plant will operate at 55 °C. Thanks to the observed equilibrium pressure at about 5.9 bar and 10.6 bar for the first and second absorption plateau, respectively [32], this alloy is suitable to absorb H_2 directly from a PEM-EL, with a supply pressure <30 bar. Then, the H_2 could be released supplying a PEM-FC at 1 bar, owing to an equilibrium pressure of about 3.1 bar and 6.8 bar for the first and second desorption plateau, respectively [32]. The production and integration of a large-scale storage plant requires preliminary stages of prototyping, including a careful evaluation of the properties of the hydrogen storage material, which can differ moving from laboratory to industrial scale production. Indeed, the design can impose both technical and economic requirements that can drastically change the sorption properties of the selected materials. In particular, the purity of the starting raw materials will be dictated by the price and availability of parent elements. Processing techniques will differ, passing from a laboratory arc or induction melting to an industrial plant. The degree of control of the oxygen level at each step changes, due to a lower grade of vacuum during the synthesis and the occurrence of steps in air at high temperatures at an industrial level, compared to the controlled atmosphere maintained during the whole process at the laboratory scale. Finally, the economic design requirements limit the possibility after the synthesis to perform heat treatments at high temperatures and for long times, such as those described in the literature for laboratory scale processing [31,32].

Therefore, the first stage for the prototyping the hydrogen storage plant was the characterization of a preliminarily batch of 5 kg of powder of a $TiFe_{0.85}Mn_{0.05}$ alloy produced at industrial level, to understand how the final hydrogen properties can be affected by the upscaling and to verify if the materials would be suitable for the final application. This work reports a detailed study of phases composition, the microstructure and hydrogen sorption properties of the industrially produced $TiFe_{0.85}Mn_{0.05}$ alloy, comparing results with those obtained on a sample with the same overall composition previously prepared by the same authors at a laboratory scale, as reported in Refs. [31,32]. The goal is to understand if the industrially prepared alloy is suitable to be used in the final plant, investigating its activation and operation at 55 °C, which is a temperature appropriate for the integration with a PEM-EL and PEM-FC, as well as its stability over cycling and its resistance to impurities in the gas supply.

Experimental

Synthesis and processing

An amount of 5 kg of $TiFe_{0.85}Mn_{0.05}$ was prepared from the parent elements by melting. Raw materials are electrolytic grade Fe and Mn and commercially pure (CP) Ti Grade 1 (minimal purity about 99.1%). The chemical composition was obtained by taking a Ti-Fe-Mn master alloy with a nominal composition of 5.8 wt.% Mn and diluting the manganese to the target composition by additions of Fe and Ti. Dilution and melting were performed in a skull melter [37] under vacuum (10^{-2} mbar). Then, the liquid alloy was poured in a water-cooled Cu-crucible. The resulting ingots were grinded in air in two steps. Firstly, the bulk was crushed in a jaw crusher to chunks, and then it was micronized in a hammer mill. The obtained powder was then poured in a sieve to select only the particle size with a dimension lower than 420 μm. Finally, the powder was delivered in air and then stored in a glovebox, under argon atmosphere with low concentration of oxygen and water (≤1 ppm).

Characterization

Chemical composition and oxygen content analysis

In the final powder form, the chemical composition of the alloy was determined with Microwave Plasma-Atomic Emission Spectrometry (MP-AES 4100 from Agilent), analysing 0.5 g, with a chemical pulping with 12 ml aqua regia and 2 ml HF. Oxygen and nitrogen contents were analysed with the elemental analyser Leco analyser ONH-863, while carbon and sulphur with the Leco CS-744.

Powder X-ray diffraction

For the as synthetized powder, Powder X-ray Diffraction (PXD) analysis was performed with a X'Pert Bragg-Brentano diffractometer, equipped with a Cu-Kα radiation and a X'celerator detector. The PXD patterns were acquired in air with an acquisition time of 1100 s per step, steps of 0.016°, from 35° to 120° in 2θ. After activation and cycling, the powders were analysed with a X'Pert Pro diffractometer in Debye-Scherrer geometry, equipped with Cu-Kα source. The powder samples were packed in glass capillaries with a diameter of 0.8 mm in a glovebox under Ar atmosphere. Measurements have been performed from 30° to 120° in 2θ, steps of 0.016° and a time per step of 400 s. Qualitative analyses were performed with the software X-Pert High Score, while Rietveld refinements of the crystal structures were carried out with the Maud software [38]. Pattern's background results to be noisy due to the fluorescence promoted by the presence of Fe in the sample and the use of Cu-Kα radiation.

Scanning Electron Microscopy

The study of the microstructure on the as synthetized sample was performed with the powder embedded in a conductive resin and polished, while morphological investigation was performed on loose powder. Analysis was carried out using a Field Emission Gun - Scanning Electron Microscopy (FEG-SEM) instrument Tescan 9000. The loose powder was also studied by performing Energy Dispersive X-ray Spectroscopy (EDX) measurements at different energy, *i.e.* 2, 5 and 15 keV, to perform Monte Carlo simulations with the software CASINO [39]. These were done to simulate the penetration depth of the beam inside the material. Finally, samples after cycling with H_2 as loose and embedded powders were studied with a SEM instrument Tescan Vega. On embedded samples, EDX elemental measurements were acquired at 20 keV.

Electron Probe Micro-Analysis

Metallographic examinations and elemental composition were obtained by Electron Probe Micro-Analysis (EPMA) with a Cameca SX100 instrument. Acceleration voltage and beam current were 15 kV and 40 mA, respectively. The as received powder was embedded in epoxy-resin and polished.

Volumetric measurements by Sievert's method

H_2 sorption properties were performed in different volumetric Sievert's apparatuses.

pcT-curves were registered with the instrument PCT-Pro by Setaram. About 2 g of sample were loaded in air and pure 6.0 hydrogen from Nippon gases was used. pcT-curves were registered maintaining the constant temperature with an electric furnace at 25, 40, 55 and 70 °C. Vacuum (10^{-3} bar) conditions were applied at about 100 °C between a curve and another, to ensure a complete hydrogen desorption.

Measurements of hydrogen sorption as a function of time were performed at 55 °C and different pressures for absorption and desorption. In addition, a long-term cycling (250 cycles) experiment was performed. A custom-made Sievert's differential pressure manometric apparatus, using 6.0 hydrogen from Linde, was used. Approximately 200 mg of sample were loaded into a stainless-steel sample holder in a glovebox under Ar atmosphere. The temperature was regulated through an electric furnace. Due to instrumental set up, in desorption it is not possible, in the entire experiment, to keep a constant pressure that slightly increases in the final part. Thus, a dynamic vacuum (10^{-3} bar) is applied to ensure a complete release of the hydrogen between the desorption and the starting of a new absorption cycle.

Furthermore, poisoning experiments were performed at 55 °C and between 25 and 1 bar, in another in-house built Sieverts-type apparatus. Ten cycles were carried out using 6.0 purity hydrogen, referred to in this paper as *"pure H_2"*, from Nippon Gases. To check the effect of contaminants on sorption properties, fourteen additional cycles were performed using 2.6 purity hydrogen, referred to as *"dirty H_2"*, from Nippon Gases. According to the supplier, the 2.6 purity hydrogen contained 50 ppm in volume of water, together with oxygen (<100 ppmV) and nitrogen (<3000 ppmV). About 1 g of powder was loaded into a stainless-steel sample holder in air.

Apparent density

Apparent density measurements were carried out inside a glovebox on as synthetized and activated powder samples. Tests were performed using a method like standard ISO 3953 [40]. However, the small quantities of sample available (*e.g.* for the activated powder) did not allow complying with all the requirements of the standard procedure. A 25 cm^3 graduated cylinder was used, carefully cleaned and dried. Samples were poured inside the cylinder and then, the cylinder was manually put in vibration until a flat level surface was formed and no further decrease in the volume of powder was noticed. The values of volumes were read on the cylinder, and those of the mass were determined by means of an analytical balance. Measurements were repeated three times and results were averaged.

Results and discussion

Chemical and structural characterization

Table 1 reports the chemical analysis for the as-synthetized powdered alloy.

Together with Ti, Fe and Mn, some N, C and S impurities are present, linked to raw materials. In addition, a non-negligible amount of oxygen is observed. The source of oxygen in the obtained powder can be linked to various steps in the process (section 2.1). Firstly, the Ti raw material of Grade 1 is already containing some oxygen. In addition, the melting process under low vacuum conditions may further promote oxygen contaminations. After melting, the obtained liquid alloy was poured in a water-cooled Cu-crucible, and a further oxygen poisoning could have been taken place. Finally, the grinding of the ingot in air to produce the powder, can be also a source of oxygen contaminations.

Fig. 1 shows the backscattered electron (BSE) image and the EDX-elemental maps for Ti, Fe, Mn and O acquired by FEG-SEM.

From the BSE image in Fig. 1, it is possible to observe two zones darker than the matrix, named Phase (1) and Phase (2). From EDX maps, it appears that, compared to the matrix, both of them are richer in Ti and poorer in Fe and Mn, especially for the darkest one, *i.e.* Phase (2). In addition, it is also possible to observe from the EDX maps that Phase (1) presents a higher content of oxygen with respect to Phase (2). According to the at.% obtained by the EDX punctual analysis (Table 2), the composition of the matrix was confirmed to be $TiFe_{0.85}Mn_{0.05}$. Concerning Phase (1), results imply an atomic ratio Ti: (Fe,Mn) equal to 2 : 1, that, from results reported in the literature, suggest the presence of a $Ti_4(Fe,Mn)_2O_x$ phase [32,34,35]. Phase (2) is the richest in Ti, and according to the elemental fractions reported in Table 2 and from results reported in the literature, it has been linked to β-$Ti_{80}(Fe,Mn)_{20}$. Indeed, for the Ti-rich samples, the occurrence of the β-$Ti_{80}(Fe,Mn)_{20}$ phase is expected, in agreement with the Ti-Fe phase diagram [33]. In contrast, $Ti_4(Fe,Mn)_2O_x$ is not expected from the phase diagram and its formation is stabilized by oxygen impurities [32,34,35]. Comparable results have been obtained performing the chemical investigation at microstructural level through EPMA analysis (Fig. S1 and Table S1). As can be seen by the BSE image of Fig. 1, $Ti_4(Fe,Mn)_2O_x$ (Phase (1)) is mainly present at grain boundaries, while the β-$Ti_{80}(Fe,Mn)_{20}$ (Phase (2)) is present as inclusions.

The PXD pattern of the as-synthetized powder (Fig. 2-a) was acquired to confirm the presence of the phases observed by SEM analysis.

The phases detected by PXD (Fig. 2-a) are in good agreement with the chemical analysis performed with the EDX. Indeed, diffraction peaks related to the presence of $TiFe_{0.85}Mn_{0.05}$, $Ti_4(Fe,Mn)_2O_x$ and β-$Ti_{80}(Fe,Mn)_{20}$ (green triangle) are observed. One diffraction peak, labelled with an orange circle and not assigned to the previous phases, was attributed to the presence of an unknown phase. Its stoichiometry is hard to assign, since only the main diffraction peak is visible with low

Table 1 – Chemical analysis on the as-synthetized alloy in powder form.

MP-AES				*Elemental analyzer*			
Ti wt.%	Fe wt.%	Mn wt.%	Others wt.%	O wt.%	N wt.%	C wt.%	S wt.%
46.60	47.09	2.72	<3.28	0.233	0.006	0.015	0.007

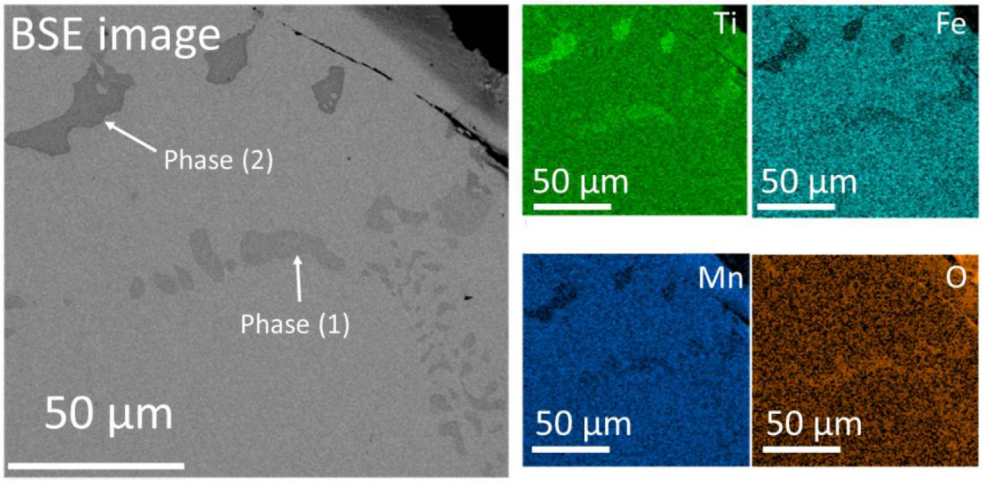

Fig. 1 – BSE image and EDX elemental maps for Ti, Fe, Mn and O, obtained by FEG-SEM on embedded as synthetized powder of the $TiFe_{0.85}Mn_{0.05}$ alloy prepared at industrial scale. The two zone darker than the matrix in the BSE image have been named Phase (1) and Phase (2) and correspond to $Ti_4(Fe,Mn)_2O_x$ and β-$Ti_{80}(Fe,Mn)_{20}$, respectively.

Table 2 – Chemical compositions in at.% obtained by EDX analysis for Ti, Fe and Mn for the $TiFe_{0.85}Mn_{0.05}$ alloy prepared at industrial scale.

	Ti (at.%)	Fe (at.%)	Mn (at.%)
Matrix	50.43 ± 3.96	45.78 ± 1.61	2.11 ± 0.44
Phase (1)	63.12 ± 1.15	34.00 ± 1.03	2.88 ± 0.12
Phase (2)	79.65 ± 0.04	16.97 ± 0.27	3.39 ± 0.32

intensity and no other phases were detected in the EDX analysis (Fig. 1). The Rietveld refinement on the experimental patterns was performed to evaluate the lattice constants and phase abundance of $Ti_4(Fe,Mn)_2O_x$ and $TiFe_{0.85}Mn_{0.05}$. β-Ti_{80}(-Fe,Mn)$_{20}$ is present in too small amount to be properly quantified. From the Rietveld refinement, 10 wt.% of Ti_4(-Fe,Mn)$_2O_x$ was detected. The $TiFe_{0.85}Mn_{0.05}$ phase has a cubic CsCl-type structure, space group $Pm\bar{3}m$, with a cell parameter a = 2.984(1) Å. Both Ti and Mn partially substitute Fe, causing a lattice expansion compared to stoichiometric TiFe, a = 2.972 Å (5). This result is in good agreement with literature for the same $TiFe_{0.85}Mn_{0.05}$ composition, *i.e.* 2.985(6) Å [31,32]. The oxide phase has a cubic structure, space group $Fd\bar{3}m$, with a cell parameter of 11.314(4) Å, in agreement with the literature [34]. The oxide $Ti_4Fe_2O_x$ has been reported in the literature with a variable composition ($0.4 \leq x \leq 1.0$) without significant changes in the lattice constant [34]. It is therefore not possible to determine accurately the stoichiometry of the oxide phase $Ti_4(Fe,Mn)_2O_x$, from the cell parameter. The evaluation of the oxygen in the stoichiometry was instead performed by calculating the elemental amount of Ti, Fe, Mn, O, from the phase abundance obtained by the refinement for different oxygen stoichiometries of the oxide. For x = 0.4, the obtained amount of singe elements (*i.e.* Ti 50.11 wt.%, Fe 47.16 wt.%, Mn 2.52 wt.%, O 0.21 wt.%) is in good agreement with the results provided by the chemical analysis reported in Table 1. Thus, according to the results of the refinement and of the chemical characterization, the stoichiometry of the oxide phase was determined to be $Ti_4(Fe,Mn)_2O_{0.4}$.

Summarising, the industrial synthesis promotes the production of an inhomogeneous sample, with secondary phases present in higher amount compared to laboratory preparation [32]. Indeed, for the same composition, the industrially prepared material contains 10 wt.% of oxide phase $Ti_4(Fe,Mn)_2O_{0.4}$, compared to 2.4 wt.% of $Ti_4Fe_2O_x$ present in sample prepared at laboratory scale [32]. In addition, the latter has also a 2.8 wt.% of β-$Ti_{80}(Fe,Mn)_{20}$, resulting in a total amount of secondary phases equal to 5.2 wt.% [32], significatively lower than that observed in the powder prepared at industrial scale.

Hydrogen sorption properties

Activation

The $TiFe_{0.85}Mn_{0.05}$ alloy prepared at laboratory scale can be easily activated after 7 h of incubation time at 25 bar H_2 and 25 °C, displaying fast hydrogen absorption kinetics [32]. On the contrary, the industrially prepared material, maintained at the same conditions of temperature and pressure, did not absorb H_2 even after 3 days. This result confirms the impact of the synthesis method on the hydrogen sorption properties of MHs [8,41]. In this case, the material with the same nominal

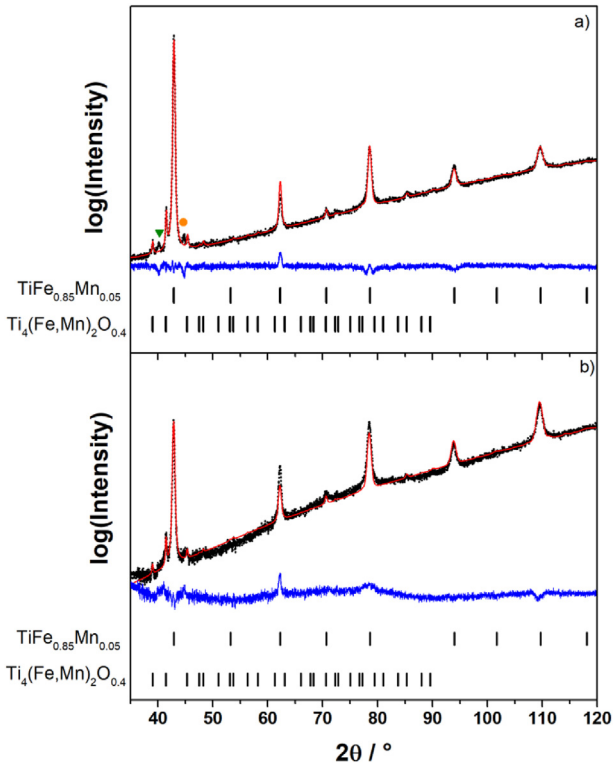

Fig. 2 – PXD patterns for the $TiFe_{0.85}Mn_{0.05}$ alloy prepared at industrial scale of (a) the as synthetized powder and (b) after activation. Dots represent experimental points, red lines the calculated patterns and blue lines the difference between them. Bars indicate diffraction peak positions for the single phases of $TiFe_{0.85}Mn_{0.05}$ (PDF-card 01-083-1635) and $Ti_4(Fe,Mn)_2O_x$ (PDF-card 01-075-0402), while the green triangle refers to β-$Ti_{80}(Fe,Mn)_{20}$ and the orange circle to an unknown phase. (For interpretation of the references to colour in this figure legend, the reader is referred to the Web version of this article.)

composition, prepared at either laboratory [32] or at industrial conditions, results in differences in phase fractions and microstructure, that strongly affect the hydrogen sorption properties, requiring the need to develop a specific activation procedure for each alloy. However, being the industrially produced powder selected as H_2-carrier for a real storage system, the activation procedure needs to fit the plant constraints (*i.e.* maximum affordable pressure and temperature), to which the system is designed to operate in safe conditions. Moreover, it is also important to optimize the activation process from an economical point of view, limiting as much as possible the H_2 consumption to reduce the costs of the start-up of the plant. Therefore, for the industrially prepared material, a specific activation procedure was developed, trying to minimize the amount of hydrogen necessary and without exceeding 100 °C and 50 bar, parameters fixed by the storage plant design to ensure efficiency and safety.

The first attempt was done by performing loading and unloading of H_2 under isothermal conditions. The powder was maintained at 90 °C at 50 bar to promote absorption and at 1 bar to promote desorption. Figs. S2–a shows a schematic representation of one activation cycle by reporting pressure and temperature as a function of time. Unfortunately, after 30 cycles of 1 h each, the activation was not achieved. On the contrary, the activation was reached by heating the powder from 25 °C up to 90 °C, temperature kept for 6 h under vacuum. Afterwards, 50 bar of H_2 were loaded under isothermal conditions at 90 °C for 4 h, cooling down the sample to 25 °C in 2 h and then keeping that temperature for 4 h. The total processing activation time is 16 h and the method requires a single hydrogen load (Figs. S2–b). Analysing by PXD a small portion of the sample after the activation and vacuum pumping (Fig. 2-b), it was observed that the oxide phase was still present in a percentage around 10 wt.%, as for the as synthetized powder (Fig. 2-a). This result suggests that the activation process is linked to a change in the morphology of the powders and in the microstructure of the alloys, rather than to a change in the phase composition, as discussed in the following section 3.2.2.

Evaluation of the apparent density

When studying a powder as H_2-carrier for a storage plant, it is of interest to evaluate the apparent density, which is a fundamental parameter for the design of the MH tank to calculate the amount of material to allocate inside the reactor. The measured apparent density represents the bulk density of the tapped powder [40]. Table 3 reports the values of apparent density obtained on the as-synthetized and activated $TiFe_{0.85}Mn_{0.05}$ powder, prepared at industrial scale.

Typically, low apparent density values imply a hindered flowability of powders, due to irregular distribution of shapes/ratios and high friction phenomena between particles. The size and its distribution also influence the apparent density, since finer powders also exhibit the abovementioned characteristics. In many cases, a decrease in density is the evidence of the formation of smaller particles [40]. Thus, according to the values reported in Table 3, the lower value of apparent density observed in the activated powder suggests only the reduction of the particle size compared to the as synthesized one [42]. In fact, comparing the PXD patterns shown in Fig. 2 before and after the activation, there are no evident variations in the phase fraction.

The different powder morphology is linked to the processing in hydrogen that tends to reduce the particle size, due to the changes in volume occurring in the transformation from the hydride to the present alloy [42]. Indeed, the role of the activation in hydrogenated powder is to crack the powder particles and promote the creation of new fresh surfaces [42]. It can be concluded that the activation procedure promotes the decrepitation of big particles into smaller ones, resulting in 17% decrease of the final apparent density. Finally, calculating the density from the structural information obtained by

Table 3 – Apparent density of the as-synthetized and activated powder for the $TiFe_{0.85}Mn_{0.05}$ alloy prepared at industrial scale.

Sample	Density g/cm^3
As received	3.94
Activated	3.28

the refinement of the PXD patterns and the chemical formula, the $TiFe_{0.85}Mn_{0.05}$ has a calculated crystal density of 6.45 g/cm^3. Thus, the apparent density of the powder before and after activation is about 60–50% of that corresponding to the crystal structure.

Thermodynamic study

pcT-curves for the $TiFe_{0.85}Mn_{0.05}$ alloy prepared at industrial scale, obtained for hydrogen absorption and desorption, are reported in Fig. 3.

Differently from what observed at a laboratory scale [31,32] (insert in Fig. 3), all pcT-curves, in both absorption and desorption, display marked sloped plateaux. The two distinct plateau pressures are not observed. Due to the slope, the values of enthalpy (ΔH) and entropy (ΔS) for the hydrogen sorption reactions have been determined from the average of values obtained by applying the Van't Hoff equation at different H_2 wt.% (*i.e.* 0.4, 0.6 and 0.8, Table S3 and Fig. S3). Results are reported in Table 4 as the average with the standard deviation, calculated by the Van't Hoff plots at the different H_2 wt.%, in comparison with data reported in Ref. [32] for the same composition prepared at laboratory scale. Thermodynamic data are in the same range of values previously reported in the literature [32].

Considering the use of the material as hydrogen carrier to be supplied by a PEM-EL at 30 bar and to feed a PEM-FC at 1 bar (orange horizontal lines in Fig. 3) at a working temperature of 55 °C, a reversible capacity of about 1.0H_2 wt.% is expected (orange vertical lines in Fig. 3), which is significantly lower than the value of 1.63H_2 wt.% observed for the same composition prepared at the laboratory scale [32], as evidenced in the insert of Fig. 3. The marked slope and the reduced capacity for the industrially prepared material are linked to the absence of the annealing treatment after alloy synthesis and to the high fraction of secondary phases, which, as already discussed in section 3.1, is almost twice compared to that observed in the material prepared at the laboratory scale [32]. In fact, the annealing treatment induces a homogenization of the composition, promoting flat plateaux [30]. On the other hand, annealing is costly and difficult to be performed at industrial level, especially for the laboratory process followed in Refs. [31,32], *i.e.* one week annealing at 1000 °C. A progressive decrease of the H_2 storage capacity was also observed by increasing the quantity of secondary phases in Ref. [32]. In this work, the discrepancy in observed hydrogen sorption properties between sample prepared at laboratory and industrial scale is due to the observed higher fraction of secondary phases. Indeed, both the oxide and β-$Ti_{80}(Fe,Mn)_{20}$ do not reversibly absorb hydrogen at the applied conditions [34], decreasing the overall reversible gravimetric capacity of the material.

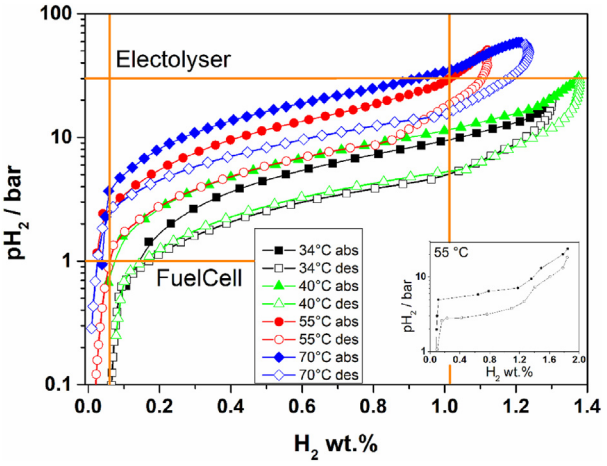

Fig. 3 – pcT-curves at 34-40-55-70 °C in absorption (full points) and desorption (empty points) for the $TiFe_{0.85}Mn_{0.05}$ alloy prepared at industrial scale, with solid lines as a guide for the eyes. The orange horizontal lines indicate the pressure of a PEM-EL with supply pressure at 30 bar and a possible desorption pressure at 1 bar for a PEM-FC. In the insert, the pcT curve at 55 °C, drawn from Ref. [32], is reported. (For interpretation of the references to colour in this figure legend, the reader is referred to the Web version of this article.)

Definition of plant conditions

To define the conditions for the large-scale hydrogen storage plant, it is fundamental to determine the proper supply and release pressure, considering the system to be integrated with a PEM-EL (<30 bar) upstream and a PEM-FC downstream (1 bar). So, the hydrogen sorption behaviour of the $TiFe_{0.85}Mn_{0.05}$ alloy prepared at industrial scale was investigated at different pressures, at the plant working temperature of 55 °C, evaluating five absorption pressures, *i.e.* 25, 20, 15, 10 and 5 bar and three desorption ones, *i.e.* 4, 2 and 1 bar (Fig. 4).

In general, for both reactions, the 90% of the gravimetric capacity is processed in less than 10 min, highlighting a fast sorption rate of selected material. Considering the storage properties in absorption, in Fig. S4, the total amount of hydrogen absorbed at different pressures at 55 °C is plotted as symbols over the measured pcT-curves. Values lays on the pcT-curve and the maximum absorption capacity increases with pressure, from 0.2H_2 wt.% at 5 bar to 1.0H_2 wt.% at 25 bar, in agreement with the thermodynamic study (Fig. 3). For desorption, the capacity can be visualized in Fig. S4. A slight increase in pressure was always observed at the end of the experiments as described in section 2.2.5. Therefore, the observed desorbed capacity is not achieving the exact value determined by thermodynamics. As an example, the desorbed amount of hydrogen from 25 bar to the starting desorption pressure of 4, 2 and 1 bar is 0.5, 0.7 and 0.8H_2 wt.%, respectively (Fig. S4). Therefore, an increase in pressure at the end of the desorption equal to 1.8 bar was occurring. It can be noticed that, for selected conditions, the pressure levels exert almost no influence on the reaction driving force. Indeed, the last fraction of all the curves in Fig. 4 is flat, suggesting that the reaction cannot proceed further due to thermodynamic constraints, rather than hindered kinetics.

These results suggest that, for the plant at the designated working temperature of 55 °C, absorption can occur directly from a PEM-EL, between 25 and 30 bar, with a storage capacity of about 1.0H_2 wt.%, in agreement with the thermodynamic study, and desorption can be achieved at 1 bar, directly supplying a PEM-FC, displaying a fast sorption rate.

Table 4 – Average enthalpy (ΔH) and entropy (ΔS) for the hydrogen sorption reactions, obtained in both absorption and desorption, for the $TiFe_{0.85}Mn_{0.05}$ alloy prepared at industrial scale. Values obtained for the same composition prepared at laboratory scale [32] are reported for comparison.

	Absorption	Desorption	Ref. [32] Absorption	Ref. [32] Desorption
ΔH $kJmol_{H2}^{-1}$	−31.2 ± 0.8	31.2 ± 1.0	1st plateau: 27.8 2nd plateau: 32.5	1st plateau: 30.6 2nd plateau: 35.2
ΔS $Jmol_{H2}^{-1}K^{-1}$	−115.7 ± 1.4	110.0 ± 1.3	1st plateau: 99 2nd plateau: 121	1st plateau: 103 2nd plateau: 126

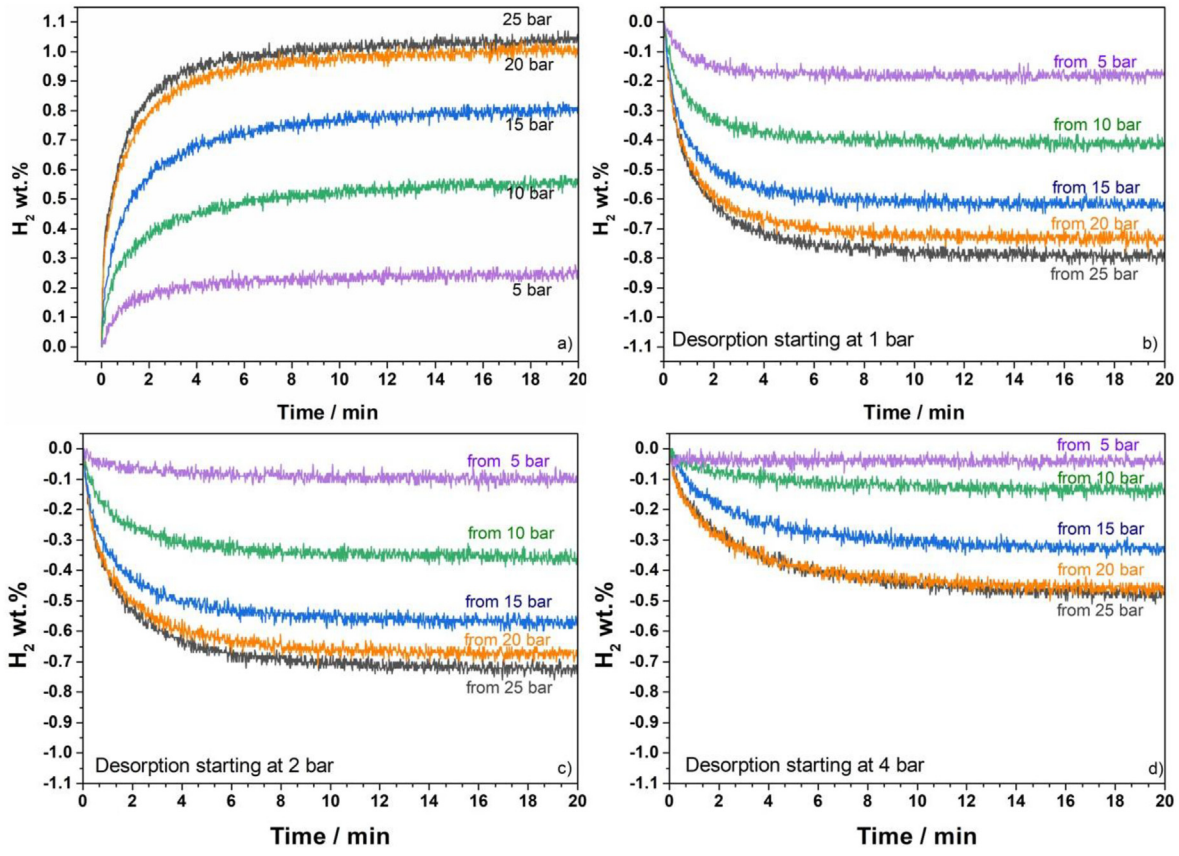

Fig. 4 – Absorption and desorption kinetic curves for the $TiFe_{0.85}Mn_{0.05}$ alloy prepared at industrial scale: (a) absorption at different pressures; (b) desorption from different pressures at 1 bar; (c) desorption at 2 bar; (d) desorption at 4 bar.

Cyclability study and resistance to gas impurities

When studying an alloy for an H_2 storage plant, the set of fundamental requirements includes its stability in performance over cycling and its resistance to possible hydrogen impurities. This makes necessary to check the expected lifetime of the material, in terms of reversible capacity and kinetic performances. So, at the defined working conditions of temperature and pressure (*i.e.* 55 °C and 25–1 bar, followed by dynamic vacuum as described in section 2.2.5), several absorption and desorption cycles were performed, to evaluate the stability of the hydrogen sorption properties of the $TiFe_{0.85}Mn_{0.05}$ alloy prepared at industrial level. As can be seen from Fig. 5, the hydrogen storage capacity remains stable at about 1.0H_2 wt.% over 250 cycles, observing even a slight increase (0.03H_2 wt.%), and confirming the excellent stability of the alloy. Then, over the 250 cycles, kinetic performances are also unaffected, with single curves almost superimposable, as shown in Fig. S5, reporting the hydrogen absorption curves taken every 50 cycles.

After more than 250 cycles with pure H_2, the powder was characterized by PXD and SEM. A comparison of the particle size of the powder after synthesis and hydrogen sorption cycles suggests that cycling promotes the reduction of the particle size. Indeed, by sieving after synthesis, the powder presents a dimension lower than 420 μm, while from a Secondary Electron SEM image on loose powder after 250 cycles (Fig. S6), the average particle size results to be lower than 200 μm. The registered PXD pattern (Fig. S7) shows that the main phase, $TiFe_{0.85}Mn_{0.05}$, is predominant, and the secondary phases detected on the as synthetized powder (Fig. 2-a) are basically maintained, observing a slight reduction of the oxide content and the evidence of a small new peak at about 35° in 2θ, linked to an unidentified phase. It is worth noting that, performing an EDX-study on the matrix phase in an

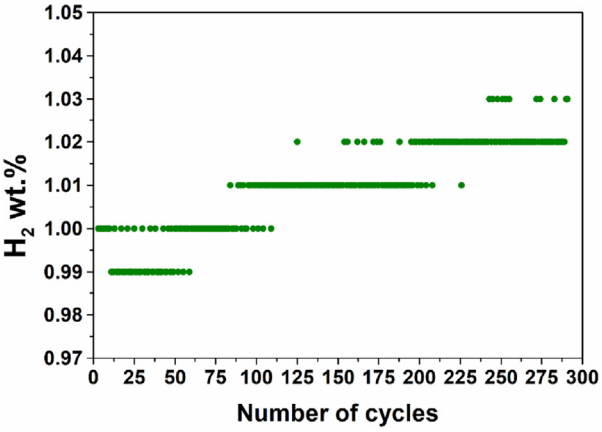

Fig. 5 – Gravimetric density (H_2 wt.%) absorbed as a function of the number of cycles for the $TiFe_{0.85}Mn_{0.05}$ alloy prepared at industrial scale. Analysis occurred at 55 °C absorbing at 25 bar.

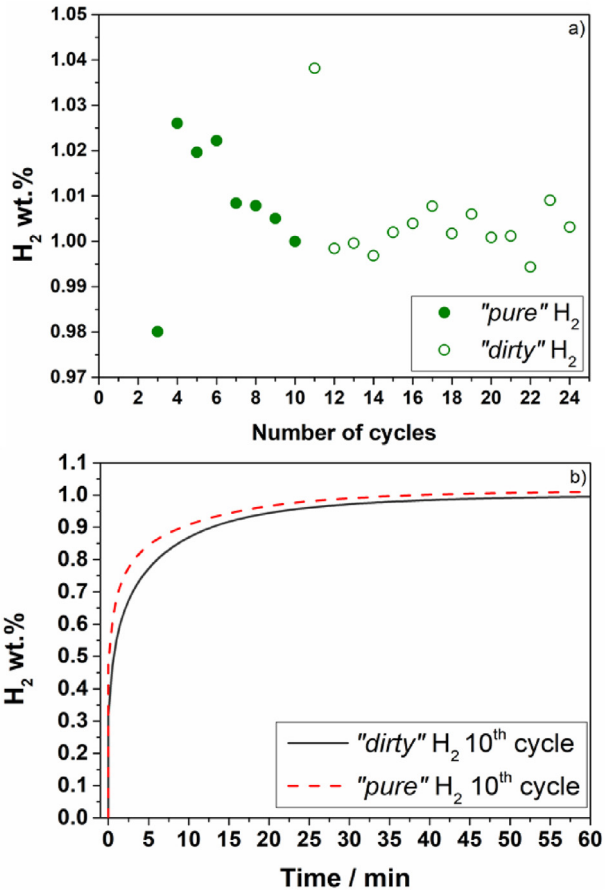

Fig. 6 – (a) Gravimetric density (H_2 wt.%) as a function of the number of cycles for the $TiFe_{0.85}Mn_{0.05}$ alloy prepared at industrial scale occurred at 55 °C absorbing at 25 bar with *"pure"* and *"dirty"* H_2; (b) Gravimetric density (H_2 wt.%) as a function of time of the absorption curves acquired for the $TiFe_{0.85}Mn_{0.05}$ alloy prepared at industrial scale at the 10th cycle with *"pure"* and *"dirty"* H_2.

embedded powder after 250 cycles, the same $TiFe_{0.85}Mn_{0.5}$ composition has been detected (Table S8).

Since, in the plant, H_2 is produced by an EL, impurities of water, oxygen and nitrogen are expected in the hydrogen flow. The effect of these contaminants on the hydrogen sorption properties were therefore evaluated by performing absorption and desorption cycles using different grades of purity of H_2. The first ten cycles were carried using *"pure H_2"* (grade 6.0), followed by fourteen cycles performed with *"dirty H_2"* (grade 2.6). The amount of H_2 absorbed on cycling with pure and dirty H_2 is shown in Fig. 6-a.

As shown in Fig. 6-a, the experiment with the two grades of purity does not indicate any significant difference in the gravimetric capacity that remains stable at about 1.0H_2 wt.%. On the other hand, the kinetic is slightly affected, as seen by comparing the absorption curve after 10 cycles with *"pure H_2"* and after 10 cycles (20 overall) with *"dirty H_2"* (Fig. 6-b). Indeed, to reach 90% of the total H_2 capacity, 10 min are necessary with *"pure H_2"*, while 15 min are necessary with the *"dirty H_2"*, in which only the 80% is processed in 10 min (Fig. 6-b). Thus, it seems that impurities slow down the reaction rate, without affecting the maximum capacity upon cycling (Fig. 6-a). Same considerations can be done for desorption (Fig. S9).

The absorption reaction mechanism was studied through the Johnson–Mehl–Avrami (JMA) model [14], which allows to identify the rate determining mechanism of reaction by plotting the reacted fraction (α) as a function of time (t), according to Equation (1):

$$ln(-ln(1-\alpha)) = lnk + mlnt \quad (1)$$

where k is a temperature-dependent rate parameter and m is a constant. Thanks to values tabulated by Hancock and Sharp [43], from the obtained value of m, it was possible to determine the rate limiting mechanism. For the absorbing reactions with *"pure"* and *"dirty"* H_2, values of α were calculated and $ln(-ln(1-\alpha))$ was plotted as a function of lnt (Fig. S10), according to Equation (1). The evaluation of the m was made considering the entire range of α, resulting in values of 0.55 and 0.61 for *"pure"* and *"dirty"* H_2, respectively. Such values are quite similar and, according to Ref. [43], they can be linked to a diffusion mechanism as rate determining step. As it can be seen from Fig. S10, all values are properly fitted in the whole range, suggesting that diffusion is the rate determining mechanism in the entire reaction. This implies that gas impurities do not affect the reaction mechanism, but it is reasonable to suppose that the slowing down is linked to the different partial pressure of H_2. In fact, as already reported in Ref. [44], the decrease of the partial pressure of H_2, due to the presence and accumulation of impurities, promotes the slowdown of the reaction in comparison to the use of high purity H_2.

The role of oxygen in material processing and its influence on sorption properties

It is reported in the literature that the role of the oxygen introduced during the synthesis of TiFe-compounds, resulting in the formation of Ti-Fe-O ternary oxides, *e.g.* $Ti_4Fe_2O_x$ with $0.4 \leq x \leq 1$, Ti_3Fe_3O or $Ti_{10}Fe_7O_3$, as secondary phases and/or as surfaces passive layer, is crucial in the sorption properties,

starting already from their activation [15,17,28,34,35,45]. Indeed, ternary Ti-Fe-O oxides are always present in TiFe-based compounds, because of the oxygen immiscibility in the TiFe-based matrix and of the titanium high affinity with O [34]. Nevertheless, different results are reported in the literature regarding the ability of these oxides to be hydrogenated and, as a consequence, on their role in the H_2 sorption properties of the TiFe-compounds. Thus, in the following, the results obtained in these works are briefly summarized to help in the understanding the hydrogen sorption behaviour of the $TiFe_{0.85}Mn_{0.05}$ alloy prepared at industrial level.

Surface oxides as passive layer can be formed because of local concentration of oxygen at the surface, resulting in non-equilibrium Ti-Fe-O species [34,46]. Regarding the surface oxidation, it is reported in Refs. [47,48] that the different electronic state of Fe in the matrix and in the surface oxide, when the material is heated, plays a catalytic role in the hydrogenation, promoting the dissociation of the hydrogen molecule. At this point the presence of grain boundaries between these oxides and passivated Ti(Fe,Mn) can act as fast channels for hydrogen diffusion, promoting alloy hydrogenation in bulk. Cracks and fresh surfaces are created by bulk expansion, helping in the hydrogenation [49–52]. The Ti_3Fe_3O and $Ti_{10}Fe_7O_3$ oxides were reported to be typical oxides present at the surface in TiFe-compounds; in particular, the Ti_3Fe_3O is reported as passive layer for the TiFe-alloys [53]. They do not absorb H_2, decreasing the storage capacity of TiFe-alloys [53–55]. On the other hand, they induce a reduction of the particle size, promoting hydrogenation. In fact, during hydrogen absorption and desorption cycles, the combination of a volume change of the matrix with the unchanged volume of the oxides enables particle size refinement [54]. Rupp et al. [34], by investigating the formation of ternary $Ti_{4-x}Fe_{2+x}O_y$ oxides in TiFe samples and their hydrogen sorption properties, concluded that these compounds are present in considerably high amount in commercial alloys, *i.e.* when industrial production is used, since high amount of oxygen can be introduced during processing. In particular, for Ti-rich compositions, the $Ti_4Fe_2O_{0.4}$ is formed. $Ti_{4-x}Fe_{2+x}O_y$ oxides were reported to absorb H_2 [34,45,56,57]. Their structure was investigated by neutron diffraction by Stioui et al. [45] and, more recently, by Density Functional Theory (DFT) calculation by Ha et al. [56]. A common result of investigations on $Ti_{4-x}Fe_{2+x}O_y$ oxides is that the oxygen content does not affect the cell parameter dimension, both in the hydrogenated and non-hydrogenated state, while it influences the amount of hydrogen absorbed. The higher the oxygen content, the lower the hydrogen storage capacity [34,45,56,57]. Several results were reported concerning the hydrogen sorption conditions (*i.e.* pressure and temperature) in $Ti_{4-x}Fe_{2+x}O_y$ oxides, but thermodynamic data are not available. Stioui et al. [45] reported easy hydrogenation of Ti_4Fe_2O at room temperature under few (not specified) bars of H_2 without need of activation. Also Rupp et al. [34] observed an easy hydrogenation between 20 °C and 100 °C under less than 1 bar of H_2 for the $Ti_4Fe_2O_{0.4}$, with a capacity of about 1.32 wt.% up to 5 bar, reaching even 1.76 wt.% in capacity hydrogenating the system at 5 bar, after cooling from 200 °C to room temperature. Hiebl et al. [57] reported a hydrogenation at 40 bar and 200 °C for $Ti_4Fe_2O_{0.46}$. It is important to point out that the easy activation and the hydrogenation at low pressures and temperatures observed in Refs. [34,45] were obtained with the oxides in bulk form, while, in powder form, the hydrogenation is reported to be harder. Indeed, Rupp et al. [34] observed a deactivation of the oxide by powdering the bulk, in agreement with Matsumoto et al. [58] and observing hydrogenation only at 40 bar and 250 °C, in agreement with ref. [57]. This change in the sorption properties observed for the $Ti_4Fe_2O_{0.4}$ is not clear, but similar behaviour was observed for β-$Ti_{80}Fe_{20}$ [34]. However, for the latter, hydrogenation in bulk form requires hard activation conditions, *i.e.* several cycles at 500 °C and 40 bar, while in powder form the hydrogenation occurs at 300 °C and 40 bar [34]. Finally, by preparing samples with different amount of $Ti_4Fe_2O_{0.4}$ and β-$Ti_{80}Fe_{20}$, together with the pure TiFe matrix, it was found that for high amount of $Ti_4Fe_2O_{0.4}$ at least 200 °C and 40 bar are required for the activation, while when β-$Ti_{80}Fe_{20}$ is present in higher amounts, hydrogenation occurs between 20 and 100 °C at 40 bar [34], in good agreement with ref. [58]. The hydrogenation of the secondary phases requires high pressures and temperatures, resulting in an overall reduction of the storage properties of the alloys, and when β-$Ti_{80}Fe_{20}$ is present in higher amount than the oxide, milder activation conditions are required [34]. Indeed, Nagai et al. in studying TiFeMn-samples, founds that the composition and the amount of the secondary phase, Ti-Fe-Mn-based, is crucial in the activation of the matrix. A proper fraction of secondary phases, even if does not absorb H_2, helps the activation thanks to its interface with the matrix acting as diffusion path for the hydrogen. The activation is emphasized only when the secondary phases are even absorbing H_2 in the activation conditions [59]. Finally, the different thermal expansion between the matrix and the secondary phases helps the hydrogenation process, promoting the cracking of the alloys [24].

Taking into account the information from the literature, it is possible to describe the sorption behaviour of the $TiFe_{0.85}Mn_{0.05}$ sample prepared in this work at industrial level. In fact, the oxygen is affecting its production, with the formation of higher amounts of $Ti_4(Fe,Mn)_2O_{0.4}$ with respect to the same nominal composition prepared at a laboratory scale [31,32], in agreement with ref. [34]. The industrial preparation introduces a high amount of oxygen, because of less pure raw materials and material processing, that can promote the formation of oxides inclusions, together with the formation of a passive layer at the surface. The formation of a passive layer at the surface can be linked to the harsher activation observed if compared to Ref. [32], considering that this passive layer is hindering the first hydrogenation, requiring a treatment in temperature and pressure to promote the diffusion through it [42]. Thus, the surface of the as synthetized material was studied by EDX analysis on loose powder with a FEG-SEM instrument, by changing the energy applied of the incident beam, *i.e.* 2, 5, and 15 keV. The rise of the energy of the incident beam implies a deeper penetration of the beam inside the material, allowing a progressive investigation of the composition of the material from the surface to the bulk [60]. The signal of the oxygen is taken as an indicator of the presence of the passive layer. Hence, if the passive layer is present, its value is expected to progressively decrease by increasing the energy, *i.e.* the penetration depth inside the matrix. The observed counts normalized by the incident energy are

reported in Fig. 7-a as a function of the emitted energy in keV, up to 1 keV. The EDX signal of oxygen occurs at about 0.5 keV and its decrease is observed by increasing the applied beam energy, confirming a change in composition between the surface and the matrix.

The thickness of the passive layer was investigated by a Monte Carlo simulation with the software CASINO [39], estimating the penetration depth of the electronic beam as a function of the applied energy. An example of results of the electron penetration inside the material is displayed in Fig. S11. As shown there, when an incident beam penetrates inside the material, the emitted signal comes from various depths. However, the more the beam penetrates inside the material, the lower the emitted signal is, passing from 90% to 5%. Thus, it was selected to consider the corresponding depth of the 90% of the emitted energy, since it represents the zone from which the majority of the information regarding the material comes from. Fig. 7-b shows the elemental amount as a function of beam penetration at 90% of the emitted energy, obtained with the Monte Carlo simulation. For the values reported in Fig. 7-b, the highest amount of oxygen is linked to a beam penetration of 8.4 nm, linked to an applied beam energy of 2 keV, while at 5 keV and 15 keV, the depth is of 15 and 123 nm, respectively. The oxygen content decreases reaching a nearly stable value already at 15 nm, accompanied by a rise for Fe, Ti and Mn content. These results suggest the occurrence of a passive layer less than 15 nm thick, and the atomic percentage obtained from the EDX analysis (Fig. 7-b) suggests a Ti:Fe:O atomic ratio equal to 3:2.5:1, *i.e.* similar to the Ti_3Fe_3O, already reported as passive layer of TiFe [53,55]. The presence of the passive layer cannot be confirmed through PXD analysis, since the penetration depth of the X-Rays calculated in the experimental conditions was estimated to be between 1 and 3 μm, significantly deeper than the value of 15 nm estimated from the Monte Carlo simulation for the EDX analysis. The presence of the $Ti_4(Fe,Mn)_2O_{0.4}$ at the surface of the powder cannot be excluded either, because of its high amount in the material. Indeed, since it was detected along grain boundaries (Fig. 1), it can remain at the surface in some cases during the decrepitation of the powder.

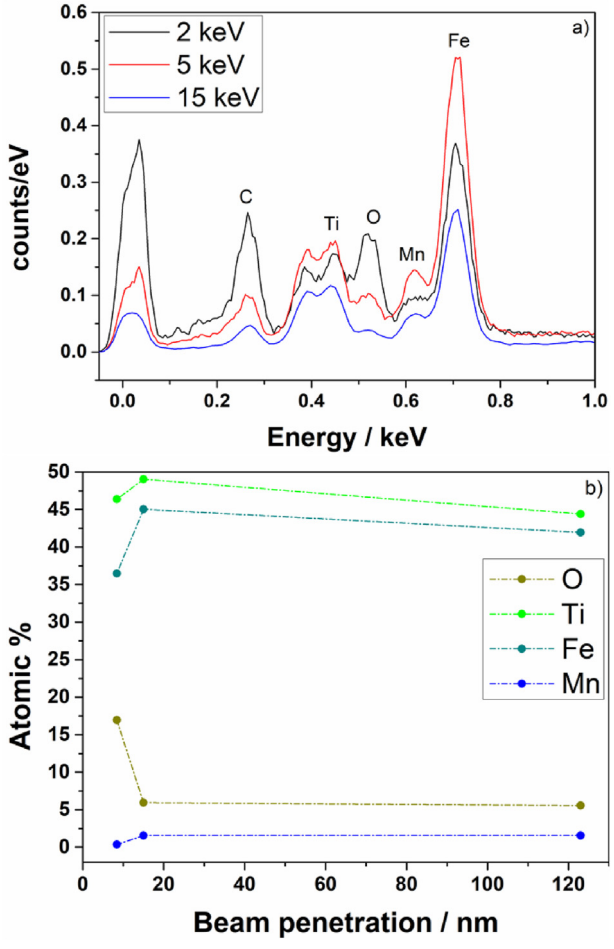

Fig. 7 – (a) EDX results, from FEG-SEM instrument, for the $TiFe_{0.85}Mn_{0.05}$ alloy prepared at industrial scale in terms of counts/eV as a function of the keV obtained with an experimental energy of 2, 5 and 15 keV; (b) the atomic percentage for Ti, Fe, Mn and O obtained by EDX analysis as a function of beam penetration at the 90% of the emitted signal per each energy applied, *i.e.* 2, 5, and 15 keV.

On the basis of the literature data previously presented, regarding the sorption behaviour of Ti-Fe-O and β-$Ti_{80}Fe_{20}$ (β-$Ti_{80}(Fe,Mn)_{20}$ in this work), and the results observed for the $TiFe_{0.85}Mn_{0.05}$ prepared in this work at industrial level, Fig. 8 shows a schematic illustrating the activation procedure (section 3.2.1).

At 25 °C and 25 bar (activation conditions of ref. [32]), the passive layer (Ti_3Fe_3O) hinders the first hydrogenation. Rising the temperature and pressure at 90 °C and 50 bar, respectively, promotes the diffusion of hydrogen through the passive layer, hydrogenating the matrix $TiFe_{0.85}Mn_{0.05}$. This process does not allow the hydrogenation of the secondary phases β-$Ti_{80}(Fe,Mn)_{20}$ and $Ti_4(Fe,Mn)_2O_{0.4}$, since higher temperature are required for a sample rich in oxide (*i.e.* 40 bar and 250 °C) [34]. However, both the passive layer, Ti_3Fe_3O, and the oxide, $Ti_4(Fe,Mn)_2O_{0.4}$, at the surface can play a crucial role during activation, by for instance, promoting a catalytic effect of the Fe [47,48] inducing the dissociation of H_2 and then, the hydrogenation of the matrix is facilitated due to the interface oxides-matrix [49–52]. The formation of new fresh surfaces occurs thanks to the variation in volume between the matrix and the oxide as unabsorbent species [54], promoting the cracking of the powder, enhanced also by the presence of β-$Ti_{80}(Fe,Mn)_{20}$ [59]. It is worth noting that a more effective activation was obtained through a thermal cycle, suggesting a synergic effect between a variation in volume promoted by the hydrogenation and the different thermal expansion, especially of the $Ti_4(Fe,Mn)_2O_{0.4}$ presents in high amount and distributed along the grain boundary (Fig. 1). During the activation, the particle size is reduced thanks to cracking promoted by the presence of the passive layer and secondary phases, causing the decrease in apparent density observed between the as synthesized and activated powder (Table 3).

The cracking of the powder allowed the formation of fresh surfaces to be hydrogenated, resulting in an activation procedure that still occurs in mild conditions and with only one thermal cycle, without exceeding the maximum affordable temperature and pressure of the plant.

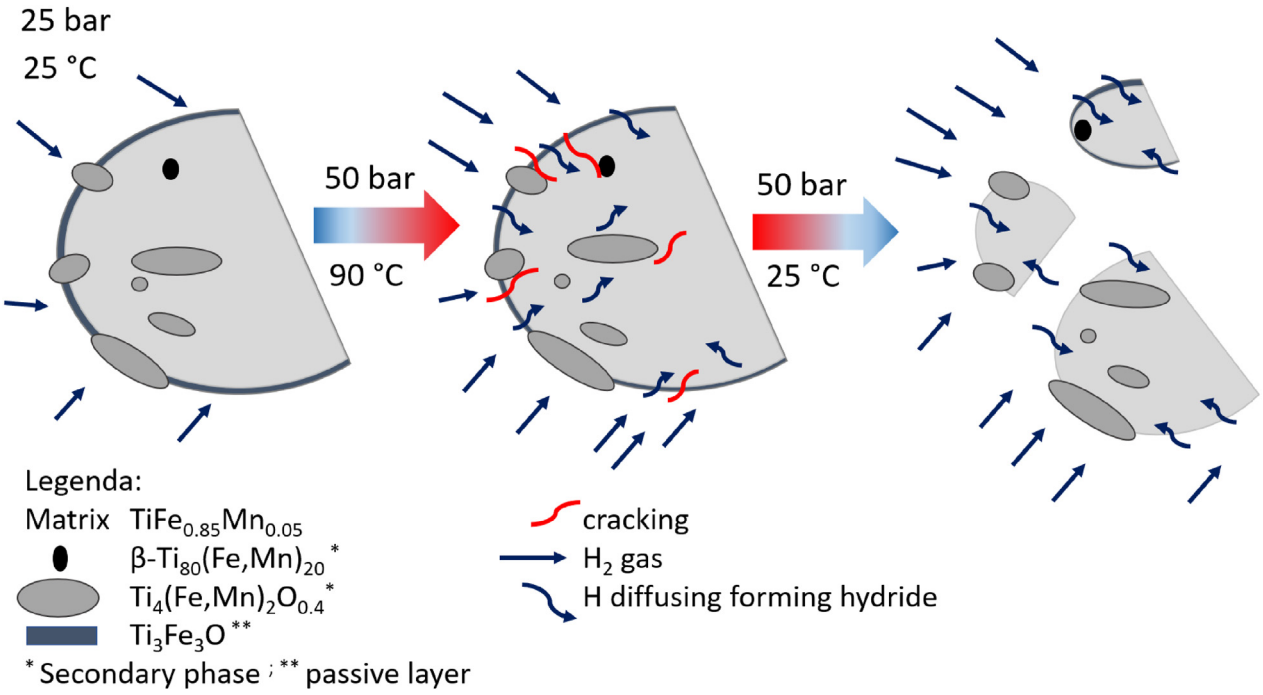

Fig. 8 – Schematic description of the activation mechanism for the $TiFe_{0.85}Mn_{0.05}$ alloy prepared at industrial scale.

The high amount of secondary phases and their inability to process hydrogen in the same condition of the $TiFe_{0.85}Mn_{0.05}$ industrially prepared [34], promoted a sensible reduction in the storage capacity, compared to the composition prepared at laboratory scale [32].

Conclusions

The $TiFe_{0.85}Mn_{0.05}$ alloy has been selected for a hydrogen storage plant and 5 kg in form of powder were prepared at industrial level by induction melting from the parent elements. Comparing results obtained in this work with the same composition prepared at laboratory [31,32] allowed to reach the following conclusions:

- A different microstructure, phase abundance and surfaces properties were observed. These differences are caused by the synthesis itself and have a strong effect on the activation procedure, sorption capacities and kinetics. In particular, the activation is harder in the sample prepared at industrial scale, as the powder needs to be heated and cooled in hydrogen atmosphere, and the storage capacity is significantly decreased.
- The thermodynamics of hydrogen sorption reactions is also affected, with a marked sloping plateau characterizing the pcT-curves of the sample prepared at industrial scale, due to the presence of secondary phase and a sample inhomogeneity. Thermodynamic characteristic plays a key role in the actual H_2 sorption rate, as the driving force at the reaction conditions is lowered by the marked slope, reducing the sorption performances.
- The hydrogen storage capacity is of 1.0H_2 wt.% at 55 °C at 25 bar and the sorption properties are maintained over 250 cycles. By using different grades of hydrogen purity, the storage capacity was not affected, while the accumulation of impurities, which changes the gas partial pressure, has a negative effect on the reaction rate.
- Considering structural and morphological characteristics, phase abundance and the observed sorption properties, the hydrogen behaviour during the activation process has been described.
- Results obtained in this work can be linked to the amount of oxygen introduced during the synthesis either from less pure Ti or from the material processing procedure, like a low grade of vacuum and the processing of the powder in air. Oxygen contaminations promoted the formation of a significant fraction of oxides as secondary phases, $Ti_4(Fe,Mn)_2O_{0.4}$, and as a passive layer, Ti_3Fe_3O.

It can be concluded that metal hydrides are strongly influenced by the synthesis method and the industrial production results in a different hydrogen sorption behaviour, that needs to be considered in order to understand if the material is suitable for the final application. The comparison between properties observed in laboratory and industrially prepared materials suggests that the amount of oxygen introduced in the synthesis should be limited, *e.g.* using high purity raw materials, that however might results in higher cost of production. The mild activation method, the fast kinetics, and the resistance to gas impurities found for the $TiFe_{0.85}Mn_{0.05}$ alloy investigated in this work, confirm its suitability as H_2-carrier for a large-scale storage plant.

Future work will be carried out in the realization of a prototype of the storage system, by producing about 50 kg of $TiFe_{0.85}Mn_{0.05}$ to investigate the alloy behaviour when integrated with a heat management.

Declaration of competing interest

The authors declare that they have no known competing financial interests or personal relationships that could have appeared to influence the work reported in this paper.

Acknowledgements

HyCARE project leading to this publication has received funding from the Fuel Cells and Hydrogen 2 Joint Undertaking (now Clean Hydrogen Partnership) under Grant Agreement No 826352. This Joint Undertaking receives 2 support from the European Union's Horizon 2020 Research and Innovation program, Hydrogen Europe and Hydrogen Europe Research.

The authors wish to thank E. Leroy for EPMA analysis, F. Couturas for his help with hydrogenation experiments and G. Fiore for the performing of the FEG-SEM analysis.

This work honours the memory of Michel Latroche, a highly respected scientist and colleague, who substantially contributed to this work and passed away in December 2021.

Appendix A. Supplementary data

Supplementary data to this article can be found online at https://doi.org/10.1016/j.ijhydene.2022.06.295.

REFERENCES

[1] Hirscher M, Yartys VA, Baricco M, Bellosta von Colbe J, Blanchard D, Bowman RC, Broom DP, Buckley CE, Chang F, Chen P, Cho YW, Crivello JC, Cuevas F, David WIF, de Jongh PE, Denys RV, Dornheim M, Felderhoff M, Filinchuk Y, Froudakis GE, Grant DM, Gray EMA, Hauback BC, He T, Humphries TD, Jensen TR, Kim S, Kojima Y, Latroche M, Li HW, Lototskyy MV, Makepeace JW, Møller KT, Naheed L, Ngene P, Noréus D, Nygård MM, ichi Orimo S, Paskevicius M, Pasquini L, Ravnsbæk DB, Veronica Sofianos M, Udovic TJ, Vegge T, Walker GS, Webb CJ, Weidenthaler C, Zlotea C. Materials for hydrogen-based energy storage – past, recent progress and future outlook. J Alloys Compd 2020;827. https://doi.org/10.1016/j.jallcom.2019.153548.

[2] Qiu S, Chu H, Zou Y, Xiang C, Xu F, Sun L. Light metal borohydrides/amides combined hydrogen storage systems: composition, structure and properties. J Mater Chem A 2017;5:25112–30. https://doi.org/10.1039/c7ta09113c.

[3] Amiri A, Shahbazian-Yassar R. Recent progress of high-entropy materials for energy storage and conversion. J Mater Chem A 2021;9:782–823. https://doi.org/10.1039/d0ta09578h.

[4] Bellosta von Colbe J, Ares J-R, Barale J, Baricco M, Buckley C, Capurso G, Gallandat N, Grant DM, Guzik MN, Jacob I, Jensen EH, Jensen T, Jepsen J, Klassen T, Lototskyy MV, Manickam K, Montone A, Puszkiel J, Sartori S, Sheppard DA, Stuart A, Walker G, Webb CJ, Yang H, Yartys V, Züttel A, Dornheim M. Application of hydrides in hydrogen storage and compression: achievements, outlook and perspectives. Int J Hydrogen Energy 2019;44. https://doi.org/10.1016/j.ijhydene.2019.01.104.

[5] Endo N, Shimoda E, Goshome K, Yamane T, Nozu T, Maeda T. Operation of a stationary hydrogen energy system using TiFe-based alloy tanks under various weather conditions. Int J Hydrogen Energy 2020;45:207–15. https://doi.org/10.1016/j.ijhydene.2019.10.240.

[6] Segawa Y, Endo N, Shimoda E, Maeda T. Pilot-scale hydrogen energy utilization system demonstration: a commercial building case study on on-site green hydrogen production and use. Int J Hydrogen Energy 2022;47:15982–91. https://doi.org/10.1016/j.ijhydene.2022.03.073.

[7] Reilly JJ, Wiswall RH. Formation and properties of iron titanium hydride. Inorg Chem 1974;13:218–22. https://doi.org/10.1021/ic50131a042.

[8] Sujan GK, Pan Z, Li H, Liang D, Alam N. An overview on TiFe intermetallic for solid-state hydrogen storage: microstructure, hydrogenation and fabrication processes. Crit Rev Solid State Mater Sci 2019:1–18. https://doi.org/10.1080/10408436.2019.1652143.

[9] Kinaci A, Aydinol MK. Ab initio investigation of FeTi-H system. Int J Hydrogen Energy 2007;32:2466–74. https://doi.org/10.1016/j.ijhydene.2006.10.006.

[10] Thompson P, Reidinger F, Reilly JJ, Corliss LM, Hastings JM. Neutron diffraction study of β-iron titanium deuteride. J Phys F Met Phys 1978;8:L75–80. https://doi.org/10.1088/0305-4608/10/2/001.

[11] Fischer P, Hälg W, Schlapbach L, Stucki F, Andresen AF. Deuterium storage in FeTi. Measurement of desorption isotherms and structural studies by means of neutron diffraction. Mater Res Bull 1978;13:931–46. https://doi.org/10.1016/0025-5408(78)90105-8.

[12] Cuevas Fermin, et al. Hydrogen storage. In: Landolt-börnstein application. Appl. - Hydrog. Technol.; 2018. p. 1–36. https://doi.org/10.1007/978-3-662-54261-3.

[13] Schober T, Westlake DG. The activation of FeTi for hydrogen storage: a different view. Scripta Metall 1981;15:913–8. https://doi.org/10.1016/0036-9748(81)90277-5.

[14] Léon A. Green energy and technology hydrogen storage. Springer; 2008.

[15] Mintz MH, Vaknin S, Biderman S, Hadari Z. Hydrides of ternary TiFexM1-x(M=Cr, Mn, Co, Ni) intermetallics. J Appl Phys 1981;52:463–7. https://doi.org/10.1063/1.329808.

[16] Dew-Hughes D. The addition of Mn and Al to the hydriding compound FeTi: range of homogeneity and lattice parameters. Metall Trans A 1980;11:1219–25. https://doi.org/10.1007/BF02668146.

[17] Pati S, Trimbake S, Vashistha M, Sharma P. Tailoring the activation behaviour and oxide resistant properties of TiFe alloys by doping with Mn. Int J Hydrogen Energy 2021;46:34830–8. https://doi.org/10.1016/j.ijhydene.2021.08.041.

[18] Fadonougbo JO, Park KB, Na T-W, Park C-S, Park H-K, Ko W-S. An integrated computational and experimental method for predicting hydrogen plateau pressures of TiFe1-xMx-based room temperature hydrides. Int J Hydrogen Energy 2022;47:17673–82. https://doi.org/10.1016/j.ijhydene.2022.03.240.

[19] Nishimiya N, Wada T, Matsumoto A, Tsutsumi K. Hydriding characteristics of zirconium-substituted FeTi. J Alloys Compd 2000;313:53–8. https://doi.org/10.1016/S0925-8388(00)01181-6.

[20] Jain P, Gosselin C, Huot J. Effect of Zr, Ni and Zr7Ni10 alloy on hydrogen storage characteristics of TiFe alloy. Int J Hydrogen Energy 2015;40:16921–7. https://doi.org/10.1016/j.ijhydene.2015.06.007.

[21] Guéguen A, Latroche M. Influence of the addition of vanadium on the hydrogenation properties of the compounds TiFe0.9Vx and TiFe0.8Mn 0.1Vx (x = 0, 0.05 and 0.1). J Alloys Compd 2011;509:5562–6. https://doi.org/10.1016/j.jallcom.2011.02.036.
[22] Nagai H, Nakatsu M, Shoji K, Tamura H. Effect of simultaneous addition of oxygen with copper or niobium on the hydriding characteristics of FeTi for hydrogen storage. J Less Common Met 1986;119:131–42. https://doi.org/10.1016/0022-5088(86)90203-1.
[23] Dematteis EM, Cuevas F, Latroche M. Hydrogen storage properties of Mn and Cu for Fe substitution in TiFe0.9 intermetallic compound. J Alloys Compd 2021;851:156075. https://doi.org/10.1016/j.jallcom.2020.156075.
[24] Dematteis EM, Berti N, Cuevas F, Latroche M, Baricco M. Substitutional effects in TiFe for hydrogen storage: a comprehensive review. Mater Adv 2021. https://doi.org/10.1039/D1MA00101A.
[25] Park KB, Fadonougbo JO, Park CS, Lee JH, Na TW, Kang HS, Ko WS, Park HK. Effect of Fe substitution on first hydrogenation kinetics of TiFe-based hydrogen storage alloys after air exposure. Int J Hydrogen Energy 2021;46:30780–9. https://doi.org/10.1016/j.ijhydene.2021.06.188.
[26] Yang T, Wang P, Xia C, Liu N, Liang C, Yin F, Li Q. Effect of chromium, manganese and yttrium on microstructure and hydrogen storage properties of TiFe-based alloy. Int J Hydrogen Energy 2020;45:12071–81. https://doi.org/10.1016/j.ijhydene.2020.02.086.
[27] Lee SM, Perng TP. Microstructural correlations with the hydrogenation kinetics of FeTi1+ξ alloys. J Alloys Compd 1991;177:107–18. https://doi.org/10.1016/0925-8388(91)90061-Y.
[28] Park KB, Na TW, Do Kim Y, Park JY, Kang JW, Kang HS, Park K, Park HK. Characterization of microstructure and surface oxide of Ti1.2Fe hydrogen storage alloy. Int J Hydrogen Energy 2021;46:13082–7. https://doi.org/10.1016/j.ijhydene.2021.01.105.
[29] Ulate-Kolitsky E, Tougas B, Huot J. Hydrogenation of TixFe2-x-based alloys with overstoichiometric Ti ratio (x = 1.1, 1.15 and 1.2). Int J Hydrogen Energy 2021;46:38363–9. https://doi.org/10.1016/j.ijhydene.2021.09.077.
[30] Johnson JR, Reilly JJ. The use of manganese substituted ferrotitanium alloys for energy storage. Altern Energy Sources 1978;8:3739–69.
[31] Challet S, Latroche M, Heurtaux F. Hydrogen Storage in TiFe(0.70+x)Mn(0.20-x) (0 <= x <= 0.15) and TiFe(0.70)Mn(0.20-y)Ni(y) (0 <= y <= 0.08) Metallic Alloys. Mater Sci Technol 2005;3:13–21.
[32] Dematteis EM, Dreistadt DM, Capurso G, Jepsen J, Cuevas F, Latroche M. Fundamental hydrogen storage properties of TiFe-alloy with partial substitution of Fe by Ti and Mn. J Alloys Compd 2021;874:159925. https://doi.org/10.1016/j.jallcom.2021.159925.
[33] Dew-Hughes D, Kaufman L. Ternary phase diagrams of the manganese-titanium-iron and the aluminum-titanium-iron systems: a comparison of computer calculations with experiment. Calphad 1979;3:175–203. https://doi.org/10.1016/0364-5916(79)90003-8.
[34] Rupp B. On the change in physical properties of Ti4−xFe2 + xOy during hydrogenation I: activation behaviour of ternary oxides Ti4−xFe2 + xOy and β-Ti. J Less Common Met 1984;104:51–63. https://doi.org/10.1016/0022-5088(84)90435-1.
[35] Davids MW, Lototskyy M. Influence of oxygen introduced in TiFe-based hydride forming alloy on its morphology, structural and hydrogen sorption properties. Int J Hydrogen Energy 2012;37:18155–62. https://doi.org/10.1016/j.ijhydene.2012.09.106.
[36] Web page. n.d. https://hycare-project.eu.
[37] Chronister DJ, Scott SW, Stickle DR, Eylon D, Froes FH. Induction skull melting of titanium and other reactive alloys. JOM (J Occup Med) 1986;38:51–4. https://doi.org/10.1007/BF03258690.
[38] Lutterotti L, Matthies S, Wenk HR, Schultz AS, Richardson JW. Combined texture and structure analysis of deformed limestone from time-of-flight neutron diffraction spectra. J Appl Phys 1997;81:594–600. https://doi.org/10.1063/1.364220.
[39] Hovington P, Drouin D, Gauvin R. CASINO: a new Monte Carlo code in C language for electron beam interaction - Part I: description of the program. Scanning 1997;19:1–14.
[40] Heaney DF. Powders for metal injection molding (MIM). In: Limited WP, editor. Handb. Met. Inject. Molding. Woodhead Publishing Limited; 2012. p. 50–63. https://doi.org/10.1533/9780857096234.1.50.
[41] Dornheim M, Doppiu S, Barkhordarian G, Boesenberg U, Klassen T, Gutfleisch O, Bormann R. Hydrogen storage in magnesium-based hydrides and hydride composites. Scripta Mater 2007;56:841–6. https://doi.org/10.1016/j.scriptamat.2007.01.003.
[42] Broon DP. Hydrogen storage materials the characterisation of their storage properties. Springer-Verlag London; 2011.
[43] Hancock JD, Sharp JH. Method of comparing solid-state kinetic data and its application to the decomposition of Kaolinite, Brucite, and BaCO3. J Am Ceram Soc 1972;55:74–7. https://doi.org/10.1111/j.1151-2916.1972.tb11213.x.
[44] Dunikov D, Borzenko V, Malyshenko S. Influence of impurities on hydrogen absorption in a metal hydride reactor. Int J Hydrogen Energy 2012;37:13843–8. https://doi.org/10.1016/j.ijhydene.2012.04.078.
[45] Stioui C, Fruchart D. Absorption d'hydrogene par Ti4Fe2O et diverses phases M6O. Mater Res Bull 1981;16:869–76.
[46] Reilly JJ, Reidinger F. Surface aggregates produced on activated FeTi as determined by X-ray diffraction. J Less Common Met 1982;85:145–53. https://doi.org/10.1016/0022-5088(82)90066-2.
[47] Schlapbach L, Seiler A, StucKi F. Surface segregation in FeTi and its catalytic effect on the hydrogenation II: AES and XPS studies. Mater Res Bull 1978;13:1031–7.
[48] Schlapbach L, Seiler A, Stucki F. A new mechanism for lengthening the lifetime of hydrogenation catalysts. Mater Res Bull 1979;14:785–90.
[49] Edalati K, Matsuda J, Arita M, Daio T, Akiba E, Horita Z. Mechanism of activation of TiFe intermetallics for hydrogen storage by severe plastic deformation using high-pressure torsion. Appl Phys Lett 2013;103. https://doi.org/10.1063/1.4823555.
[50] Schober T. On the activation of FeTi for hydrogen storage. J Less Common Met 1983;89:63–70. https://doi.org/10.1016/0022-5088(83)90249-7.
[51] Edalati K, Akiba E, Horita Z. High-pressure torsion for new hydrogen storage materials. Sci Technol Adv Mater 2018;19:185–93. https://doi.org/10.1080/14686996.2018.1435131.
[52] Modi P, Aguey-Zinsou KF. Titanium-iron-manganese (TiFe0.85Mn0.15) alloy for hydrogen storage: reactivation upon oxidation. Int J Hydrogen Energy 2019;44:16757–64. https://doi.org/10.1016/j.ijhydene.2019.05.005.
[53] Pande CS, Pick MA, Sabatini RL. The "activation" of FeTi for hydrogen absorption; an electron microscopic study. Scr Met URGICA 1980;14:899–903.
[54] Sandrock GD. The metallurgy and production of rechargeable hydrides. In: Hydrides for energy storage; 1978. p. 353–93.

[55] Pick MA, Wenzl H. Physical metallurgy of FeTi-hydride and its behaviour in a hydrogen storage container. Int J Hydrogen Energy 1977;1:413–20.
[56] Ha T, Cho YW, Lee S-I, Suh J-Y, Lee J, Shim J-H, Lee Y-S. Hydrogen occupation in Ti4M2Oy compounds (M=Fe, Co, Ni, Cu, and y = 0, 1) and their hydrogen storage characteristics. J Alloys Compd 2021;891:162050. https://doi.org/10.1016/j.jallcom.2021.162050.
[57] Hiebl K, Tuscher E, Bittner H. Untersuchungen an Hydriden im Bereich der ~-Phase Ti4Fe20. Monatshefte Fiir Chemie 1979;110:9–19.
[58] Matsumoto T, Amano M, Sasaki Y. Hydrogenation of FeTi-based alloys containing β-Ti. J Less Common Met 1982;88:443–9. https://doi.org/10.1016/0022-5088(82)90255-7.
[59] Nagai H, Kitagaki K, Shoji K. Microstructure and hydriding characteristics of FeTi alloys containing manganese. J Less Common Met 1987;134:275–86. https://doi.org/10.1016/0022-5088(87)90567-4.
[60] Goldstein JI, Newbury DE, Echlin P, Joy DC, Roming AD, Lyman CE, et al. Scanning electron microscopy and X-ray microanalysis. 2nd edition. Springer; 1992.